



# Monolithic NF@ZnO/Au@ZIF-8 photocatalyst with strong photo-thermal-magnetic coupling and selective-breathing effects for boosted conversion of CO<sub>2</sub> to CH<sub>4</sub>



Zhu Tang <sup>a</sup>, Fengfan Zhu <sup>a</sup>, Jiancheng Zhou <sup>a</sup>, Wenshuai Chen <sup>b,\*</sup>, Ke Wang <sup>a</sup>, Maochang Liu <sup>c,\*</sup>, Nan Wang <sup>a</sup>, Naixu Li <sup>a,d, \*\*</sup>

<sup>a</sup> School of Chemistry and Chemical Engineering, Southeast University, No.2 Dongnandaxue Road, Nanjing 211189, Jiangsu, PR China

<sup>b</sup> Key Laboratory of Bio-Based Material Science and Technology, Ministry of Education, Northeast Forestry University, No. 26 Hexing Road, Harbin 150040, PR China

<sup>c</sup> International Research Center for Renewable Energy, State Key Laboratory of Multiphase Flow in Power Engineering, Xi'an Jiaotong University, No.28 Xianning West Road, Xi'an, Shaanxi 710049, PR China

<sup>d</sup> Jiangsu Key Laboratory for Biomass Energy and Material, No.16 Suojin Wucun, Nanjing, Jiangsu Province 210042, PR China

## ARTICLE INFO

### Keywords:

Photocatalysis  
External fields  
Monolithic catalysts  
ZnO  
CO<sub>2</sub> reduction

## ABSTRACT

Gas adsorption/desorption process and conversion efficiency of solar energy are crucial to photocatalytic CO<sub>2</sub> conversion. Here, we report the synthesis of a metal-organic-framework based monolithic NF@ZnO/Au@ZIF-8 photocatalyst that can simulate the respiratory process to accelerate adsorption of CO<sub>2</sub> and desorption of CH<sub>4</sub> during the photocatalytic reaction. Particularly, this selective-breathing monolithic photocatalyst could coupling external magnetic field into the photocatalytic process, achieving photo-thermal-magnetic field synergy in the reaction system. Upon this photo-thermal-magnetic coupling, the temperature of surface reaction could be elevated to about 180 °C, leading to a drastically improved charge transfer behavior and the significantly increased breathing efficiency. The yield of CH<sub>4</sub> over the selective-breathing monolithic NF@ZnO/Au@ZIF-8 photocatalyst reaches 270.02 μmol/g with a high stability and a high selectivity up to 89.72%. This study provides an ideal approach for the design of monolithic catalysts not only with balanced gas adsorption-desorption property, but also endowed with multi-field coupling ability.

## 1. Introduction

With the aggravation of the greenhouse effect, the concentration of carbon dioxide in atmospheric environment continues to rise at a high speed, revealing the deep-seated contradiction between human and nature. Therefore, finding effective ways to capture or transform carbon dioxide to reduce emissions has become a top priority for human beings. Among various reduction methods for capturing and converting carbon dioxide, the photocatalytic reduction method using CO<sub>2</sub> and H<sub>2</sub>O as raw materials has aroused extensive attention due to its green and economic merits [1]. In recent years, researchers have devoted themselves to developing various types of catalysts for photocatalytic reduction of CO<sub>2</sub>. The most common materials are doped TiO<sub>2</sub>, ZnO, g-C<sub>3</sub>N<sub>4</sub> and perovskite. However, these traditional powder nanocatalysts have some shortcomings, such as easy aggregation, poor durability, and being

unexpectedly released into the environment, which seriously hinder their practical photocatalytic performance and application [2–4]. Therefore, in order to effectively prevent the formation of undesirable aggregation or release of nanocatalysts into the environment, and to maintain their good activity, they need to be fixed on the surface of a suitable substrate or frame with an open-pored structure [5–7].

Monolithic catalysts with porous framework, stable morphology and great electronic transmission performance are attractive in catalysis. Blanco and co-workers performed gas-solid heterogeneous photocatalytic oxidation of toluene and xylene on titanium dioxide-based monolithic catalyst [8]. Yi and co-workers used AgI/TiO<sub>2</sub> monolithic catalyst to degrade acid orange II, which exhibited great photocatalytic activity in visible light [9]. Liu and co-workers found that the monolithic CdS-NiS<sub>x</sub>/NF catalyst showed excellent activity, and its rate of photocatalytic hydrogen evolution was six times higher than that of

\* Corresponding authors.

\*\* Corresponding author at: School of Chemistry and Chemical Engineering, Southeast University, No.2 Dongnandaxue Road, Nanjing 211189, Jiangsu, PR China.

E-mail addresses: [chenwenshuai@nefu.edu.cn](mailto:chenwenshuai@nefu.edu.cn) (W. Chen), [maochangliu@mail.xjtu.edu.cn](mailto:maochangliu@mail.xjtu.edu.cn) (M. Liu), [naixuli@seu.edu.cn](mailto:naixuli@seu.edu.cn) (N. Li).

traditional powder of CdS [10]. Among many materials, Ni foam (NF) has a unique three-dimensional platform for electron transmission, good chemical/physical stability and high electron mobility, which is very suitable for being used as a carrier of monolithic photocatalyst [11]. ZnO has the advantages of direct bandgap, stable physical and chemical properties, low cost and good crystallinity, and it is an ideal substrate for monolithic photocatalyst [12]. Due to the synergistic effect of easy diffusion of pollutants and rapid response of the active sites, Zhang and co-workers demonstrated that Ag NPs/ZnO NAS/NiF has the highest activity of degrading the target contaminants [13].

However, there are some problems that seriously affect the photocatalytic performance of ZnO catalysts: (i) recombination of photo-generated electron-hole pairs, (ii) poor absorption of visible light, (iii) low adsorption efficiency of CO<sub>2</sub>. Most semiconductor-based photocatalysts usually have shortcomings such as the recombination of photogenerated charge carriers and sluggish kinetics of surface reaction, which can be overcome by the surface modification [14]. It has been reported that the modification of ZnO by precious metals improves the charge separation and transfer process, and enhances its photocatalytic efficiency [15–17]. Xi and co-workers reported a design of core-shell semiconductor with PtCu co-modified which has a great activity of photocatalytic conversion of CO<sub>2</sub> to CH<sub>4</sub> [18]. To solve the first two problems, Gold (Au), as a precious metal, can not only effectively separate electron-hole pairs, but also has a surface plasmon resonance (SPR) effect under visible light, which makes better use of light energy. In addition, Au can adsorb CO and activate photocatalytic reaction. Because of the structure of ZnO/Au, the selectivity of CH<sub>4</sub> can be significantly improved [19,20]. Undoubtedly, CO<sub>2</sub> adsorption is an important step in the reaction of CO<sub>2</sub> and photocatalytic conversion. In existing MOFs, the imidazole framework-8 (ZIF-8) molecular sieve has been extensively investigated for its large specific surface area, great chemical stability and excellent adsorption capacity of CO<sub>2</sub> [21]. According to previous research, Nordin and co-workers used ZIF-8 to achieve the efficient separation of CO<sub>2</sub> and CH<sub>4</sub> [22]. To solve the problem of low adsorption efficiency of CO<sub>2</sub>, we have constructed the selective-breathing monolithic NF@ZnO/Au@ZIF-8 photocatalyst, and used the selective-breathing effect of the catalyst to boost adsorbing CO<sub>2</sub>, thus enhancing the conversion efficiency.

In recent years, the introduction of external field to improve the performance of catalysts has attracted extensive attention. Because solar energy has the characteristics of the broad-spectrum, wide-area, low-energy density and intermittence, the introduction of external fields can compensate for its inability to achieve continuous high-intensity energy output [23]. For example, Wang and co-workers found that the introduction of a directional electric field can improve the actual performance of photocatalysis and increase the conversion efficiency of solar energy [24]. So far, heat, ultrasonic, microwave and electric field have been successfully introduced into some photocatalytic systems, leading to a significant improvement in photocatalytic efficiency [25–28]. Zhu and co-workers found that the magnetic field can change the chemical reaction rate and the yield of the product, and the magnetic Lorentz force can cause the expansion of the catalytic reaction area [29]. Li and co-workers demonstrated that the charge carriers can migrate to the surface reaction sites faster under the magnetic field, and more carriers can participate in the surface reaction per unit time, which helps to improve the photocatalytic efficiency [30]. Ghoussoub and co-workers illustrated that photothermal catalysis stimulates thermochemical and photochemical processes combining, and extensively promote photocatalytic efficiency [31]. To solve the problem of low utilization rate due to low energy density and intermittence of solar energy, our group previously reported a photo-thermal-magnetic coupling reaction system, which is used to improve the efficiency of photocatalytic reduction of CO<sub>2</sub> [32].

Herein, in this paper, we investigated the phenomena and mechanisms of photocatalytic reactions of the selective-breathing monolithic NF@ZnO/Au@ZIF-8 catalyst under the photo-thermal-magnetic

coupling reaction system. A series of characterization experiments were aimed at explain the excellent performance of NF@ZnO/Au@ZIF-8 photocatalytic conversion of CO<sub>2</sub> and high selectivity of CH<sub>4</sub> from three aspects: the structural characteristics, the breathing process of gas selective adsorption/desorption and the effect of photo-thermal-magnetic coupling reaction system.

## 2. Experimental

### 2.1. Materials

Hexamethylenetetramine (HMTA, C<sub>6</sub>H<sub>12</sub>N<sub>4</sub>, AR), Potassium hydroxide (KOH, AR), Ethanol (C<sub>2</sub>H<sub>5</sub>OH, AR), Zinc nitrate hydrate (Zn (NO<sub>3</sub>)<sub>2</sub>·6 H<sub>2</sub>O, AR), Chloroauric acid (HAuCl<sub>4</sub>, AR), Zinc acetate dihydrate (Zn(CH<sub>3</sub>COO)<sub>2</sub>·2H<sub>2</sub>O, AR), Hydrochloric acid (HCl, AR) and 2-methylimidazole (Hmim, AR), were gained from Sinopharm Chemical Reagent Co., Ltd. (Shanghai, China). Ni foam was obtained from Kun Shan Electronic Material Co., Ltd. (China). Mixed gas containing carbon dioxide and nitrogen (CO<sub>2</sub>: N<sub>2</sub> = 1: 99) was obtained from Nanjing Shangyuan industrial gas plant.

### 2.2. Preparation of the monolithic NF@ZnO photocatalysts

In order to make the ZnO nanorods grow more stably on the Ni Foam (2.8\*3.5 cm), a layer of ZnO seed must be grown on the surface of Ni foam first. The solution of ZnO seed was produced by mixing 1.234 g Zn (CH<sub>3</sub>COO)<sub>2</sub>·2H<sub>2</sub>O and 0.474 g KOH in 100 mL ethanol at 75 °C for 4 h. Then the Ni foam was soaked in the prepared solution of ZnO seed for 4 h. Subsequently, the ZnO seed-coated Ni foam annealed at 240 °C for 2 h and was soaked in 80 mL solution containing an equimolar Zn(NO<sub>3</sub>)<sub>2</sub>·6 H<sub>2</sub>O (2.0 mmol) and HMTA (2.0 mmol) at 85 °C for 8 h. Finally, the prepared sample was washed with deionized water and dried at 80 °C. For comparison, the ZnO powder catalysts were also prepared under the same conditions by similar steps.

### 2.3. Preparation of the monolithic NF@ZnO/Au photocatalysts

To prepare a monolithic NF@ZnO/Au photocatalyst, a widely reported photoreduction method was employed for the preparation of Au particles on the substrate [33]. In brief, a monolithic NF@ZnO photocatalyst was suspended in 10 mM HAuCl<sub>4</sub> solution and irradiated with UV-visible light (300 W Xe lamp) for 0.5 h. Finally, the obtained sample was washed with deionized water and dried at 80 °C.

### 2.4. Preparation of the monolithic NF@ZnO/Au@ZIF-8 photocatalysts

The monolithic NF@ZnO/Au photocatalyst was soaked in 30 mL of Hmim solution (3.66 M). Then, after aged for 4–48 h, the monolithic NF@ZnO/Au@ZIF-8 photocatalyst was obtained. The monolithic NF@ZnO/Au@ZIF-8 photocatalyst was washed with deionized water and dried at 80 °C. As a comparison, expect that the NF@ZnO were used instead of the NF@ZnO/Au photocatalyst, the monolithic NF@ZnO@ZIF-8 catalysts were prepared under the identical conditions by a similar process. In addition, ZIF-8 crystals were also prepared for comparison by following a previously reported procedures [34].

### 2.5. Characterizations

The samples are characterized by field emission scanning electron microscopy (SEM), transmission electron microscopy (TEM), high-resolution transmission electron microscopy (HRTEM), energy-dispersive X-ray spectroscopy (EDS) elemental mappings, X-ray diffraction (XRD) patterns, nitrogen adsorption/desorption isotherms, X-ray photoelectron spectroscopy (XPS), CO<sub>2</sub>/CO-temperature-programmed desorption (CO<sub>2</sub>/CO-TPD), UV-visible diffuse reflectance spectra (UV-visible spectra), steady-state and time-resolved

photoluminescence (PL) spectra. The gas ( $\text{CO}_2/\text{CO}/\text{CH}_4/\text{N}_2$ ) adsorption capacities were measured by static volumetric method. The temperature of the catalyst surface was measured by infrared thermometer (Smart-sensor, AS872D-01). The photoelectrochemical properties were analyzed by amperometric I-t curves (transient photocurrent), linear sweep voltammetry (LSV) curve and electrochemical impedance spectroscopy (EIS). Due to the limitation of experimental conditions, the sample was scraped off the substrate (Ni foam) and tested for TEM, XPS, UV-visible spectra,  $\text{N}_2$  adsorption/desorption isotherms,  $\text{CO}_2/\text{CO}/\text{CH}_4/\text{N}_2$  adsorption capacity and  $\text{CO}_2/\text{CO}$ -TPD testing.

## 2.6. Photocatalytic and photoelectrochemical measurements

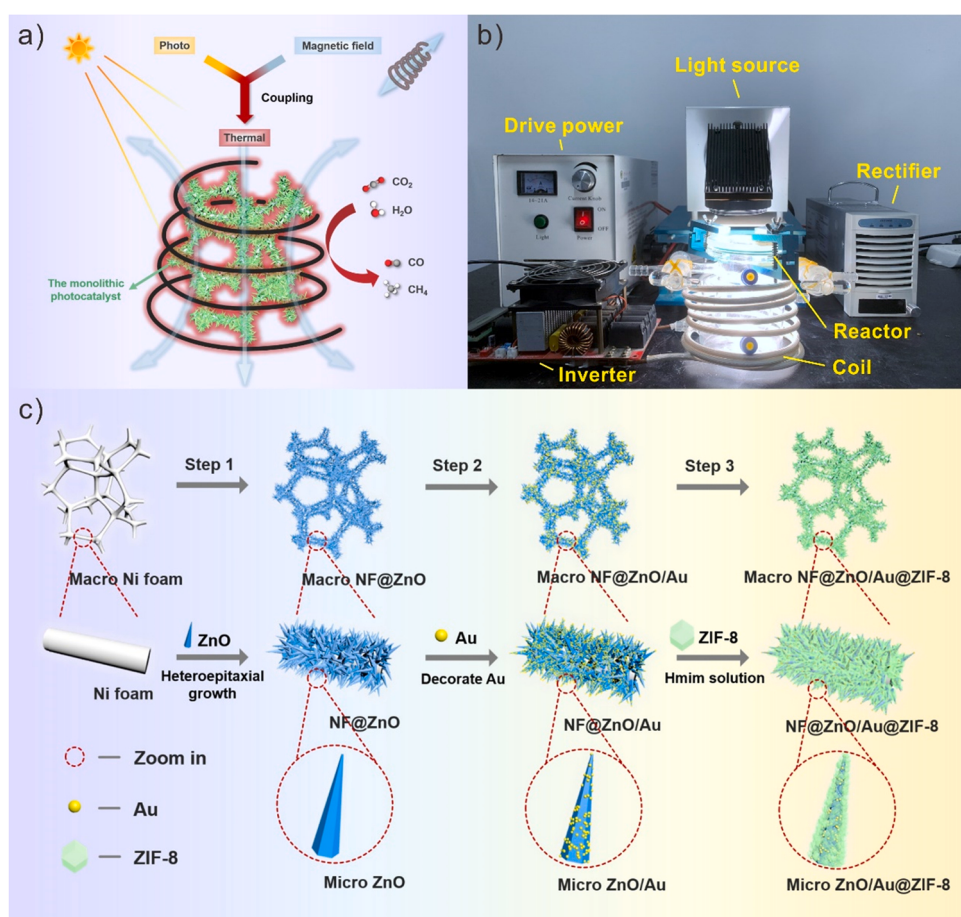
$\text{CO}_2$  reduction was performed in a 100 mL photocatalytic reactor. The sealed reactor was placed in an alternating magnetic field (AMF) generator with a frequency of 100 kHz and an intensity of 5 mT and irradiated with UV-visible light (300 W Xe lamp). The gas composition in the reactor was sampled every 0.5 h and analyzed by gas chromatography (GC-9860-5 C). A gas chromatograph-mass spectrometer (GC-MS, 7890 A and 5975 C, Agilent) was used for the  $^{13}\text{C}$  isotope labeling experiments. The functional groups and reaction mechanisms on the surface of the prepared photocatalysts were investigated by diffused mechanism infrared fourier transform spectroscopy (DRIFTS, Thermo Fisher, Nicolet 5700). Photoelectrochemical measurements (LSV, EIS, I-t curves) were performed in a standard three-electrode system with a neutral aqueous solution (0.1 M  $\text{Na}_2\text{SO}_4$ ) using a CHI660E electrochemical workstation (Chenhua Instrument). A saturated calomel electrode (SCE) and a Pt foil electrode were used as the reference electrode and counter electrode, respectively. The monolithic photocatalyst with

Ni foam was used as the working electrode.

## 3. Results and discussion

### 3.1. Structural and morphological characterizations

**Scheme 1a** shows a schematic diagram of photoreduction of  $\text{CO}_2$  by a monolithic catalyst in a photo-thermal-magnetic coupling reaction system. Magnetic heat is generated by introducing an alternating magnetic field, which works together with photothermal catalysis to form a photo-thermal-magnetic coupling synergistic catalysis. As shown in **Scheme 1b**, the photo-thermal-magnetic reaction device used in our actual reaction process consists of drive power, light source, rectifier, reactor, inverter and coil. To maximize the catalytic effect of photocatalysts in the photo-thermal-magnetic coupling reaction system, it is necessary to design a special construction of the monolithic catalyst. As is shown schematically in **Scheme 1c**, manufacturing process of selective-breathing monolithic  $\text{NF}@\text{ZnO}/\text{Au}@\text{ZIF-8}$  photocatalyst can be simply divided into three steps. Firstly, the monolithic  $\text{NF}@\text{ZnO}$  photocatalyst was prepared through an improved heteroepitaxial growth method. Ni foam did not participate in the reaction due to its stable physical and chemical properties. Therefore, the quality of the  $\text{ZnO}$  supported on the nickel foam can be obtained by drying the sample and weighing the difference before and after the reaction (Table S4). Subsequently, the Au particles were loaded on the monolithic  $\text{NF}@\text{ZnO}$  photocatalyst uniformly by a photocatalytic reduction method. By changing the dosage of  $\text{HAuCl}_4$  in the solution, the loading amount of Au particles can be controlled flexibly. Finally, the monolithic  $\text{NF}@\text{ZnO}/\text{Au}@\text{ZIF-8}$  photocatalyst can be obtained by placing the sample in the Hmim aqueous



**Scheme 1.** (a) The schematic diagram of a photo-thermal-magnetic coupled reaction system. (b) The photograph of photo-thermal-magnetic coupling reaction device. (c) The fabrication process of the monolithic  $\text{NF}@\text{ZnO}/\text{Au}@\text{ZIF-8}$  photocatalyst.

solution by in-situ self-assembly. Thus, we obtained the monolithic core-shell NF@ZnO/Au@ZIF-8 photocatalyst with Au and ZIF-8 co-modified.

The microstructure and morphology of the photocatalysts were investigated by SEM and TEM. As shown in Fig. S1a, the Ni foam presents an open porous structure with large pore-size distribution, which is very suitable as a substrate for monolithic catalysts. Fig. 1a shows the morphology of the NF@ZnO photocatalyst with ZnO nanorods densely

wrapped around the skeleton of the Ni foam. It can be clearly seen in Fig. 1b-c that ZnO on the Ni foam features hexagonal rods with average length of 1–2  $\mu$ m and diameters of about 200–300 nm. After loading Au nanoparticles, the monolithic NF@ZnO/Au catalyst retains the original morphology in macroscopic view (Fig. 1d). However, at the microscopic scale, Fig. 1e shows that many nanoparticles are distributed on the original smooth surface of ZnO. This phenomenon can be perceived

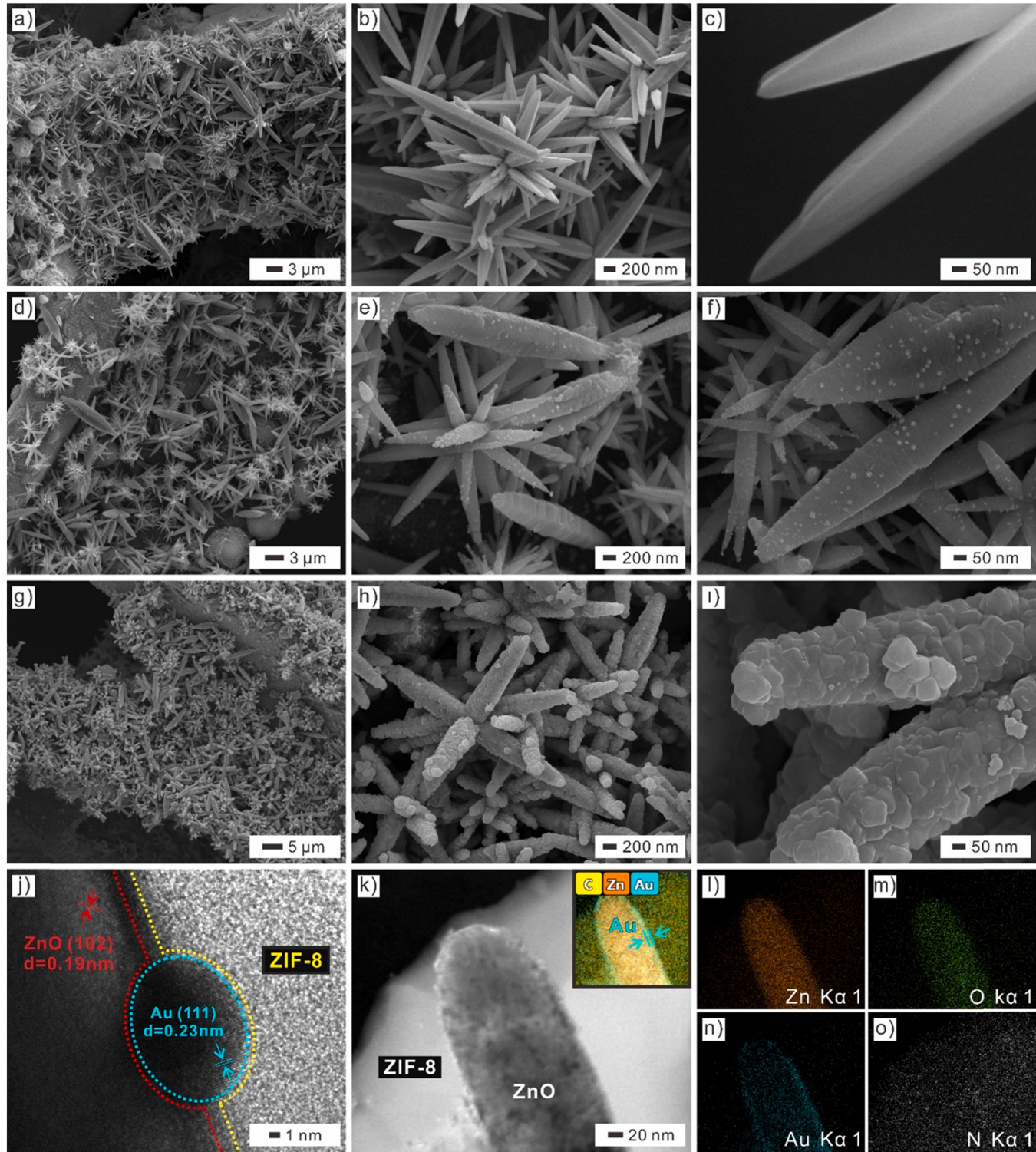


**Fig. 1.** SEM images of (a-c) the NF@ZnO catalyst, (d-e) the NF@ZnO/Au catalyst, (g-i) the NF@ZnO/Au@ZIF-8 catalyst; (j) HRTEM images of the NF@ZnO@ZIF-8 catalyst. (k) TEM images of the NF@ZnO/Au@ZIF-8 catalyst, (l-n) EDS images of Zn, O, Au, and N of the NF@ZnO/Au@ZIF-8 catalyst. Inset in (k) shows the particular distributions of C, Zn and Au of the NF@ZnO/Au@ZIF-8 catalyst.

obviously in the magnified SEM (Fig. 1f). After loading a layer of ZIF-8, the monolithic NF@ZnO/Au@ZIF-8 catalyst still maintains the rod-shaped characteristics and is densely distributed on the surface of Ni foam (Fig. 1g). Notably, compared with ZnO or ZnO/Au nanorods, the diameters of ZnO/Au@ZIF-8 nanorods (300–400 nm) are larger (Fig. 1h). In Fig. 1i, the ZIF-8 layer is distributed on the surface of ZnO/Au with a 12-sided block structure with a diameter of about 50 nm. As illustrated in Fig. 1j, the structure of ZnO/Au@ZIF-8 is more clearly seen in the HRTEM image. The measured distances of 0.23 and 0.19 nm are observed from the figure, which correspond to the (111) plane of Au and the (102) plane of ZnO, respectively. Therefore, the existence of ZnO and Au is confirmed. Au particles with a size of about 10–20 nm are loaded on the surface of ZnO. As shown in Fig. 1k-o, the structural features can be seen in HAADF and EDS images. As in the previous analysis, Au nanoparticles are widely distributed at the junction of ZnO and ZIF-8 overlayer (Inset in Fig. 1k). In addition, in the EDS image, it can be well confirmed that N as the characteristic element of ZIF-8 is distributed in the outer layer of ZnO, which clearly demonstrates the core-shell

structure. According to the above analysis, the monolithic NF@ZnO/Au@ZIF-8 photocatalyst is co-modified by Au particles and ZIF-8 layers with a core-shell structure.

### 3.2. Photocatalytic performance for $\text{CO}_2$ reduction

To investigate different catalyst structures on the photocatalytic performance, the yields of different monolithic catalysts are compared in Fig. 2a. ZIF-8 has no obvious yield under illumination, which indicates that it has no good photocatalytic performance. After loading ZIF-8 on NF@ZnO, the yields of CO and CH<sub>4</sub> with NF@ZnO@ZIF-8 (12.83  $\mu\text{mol/g}$ , 3.06  $\mu\text{mol/g}$ ) were significantly higher than those of NF@ZnO (4.57  $\mu\text{mol/g}$ , 0.56  $\mu\text{mol/g}$ ). This may be because  $\text{CO}_2$  adsorption capacity of ZIF-8 greatly improves the photocatalytic  $\text{CO}_2$  conversion of catalysts. Compared with NF@ZnO, the product yields (CO: 11.07  $\mu\text{mol/g}$ , CH<sub>4</sub>: 17.82  $\mu\text{mol/g}$ ) and the selectivity of CH<sub>4</sub> (55.25%) were significantly improved after loading Au particles. It indicates that the addition of Au plays an essential role in changing the

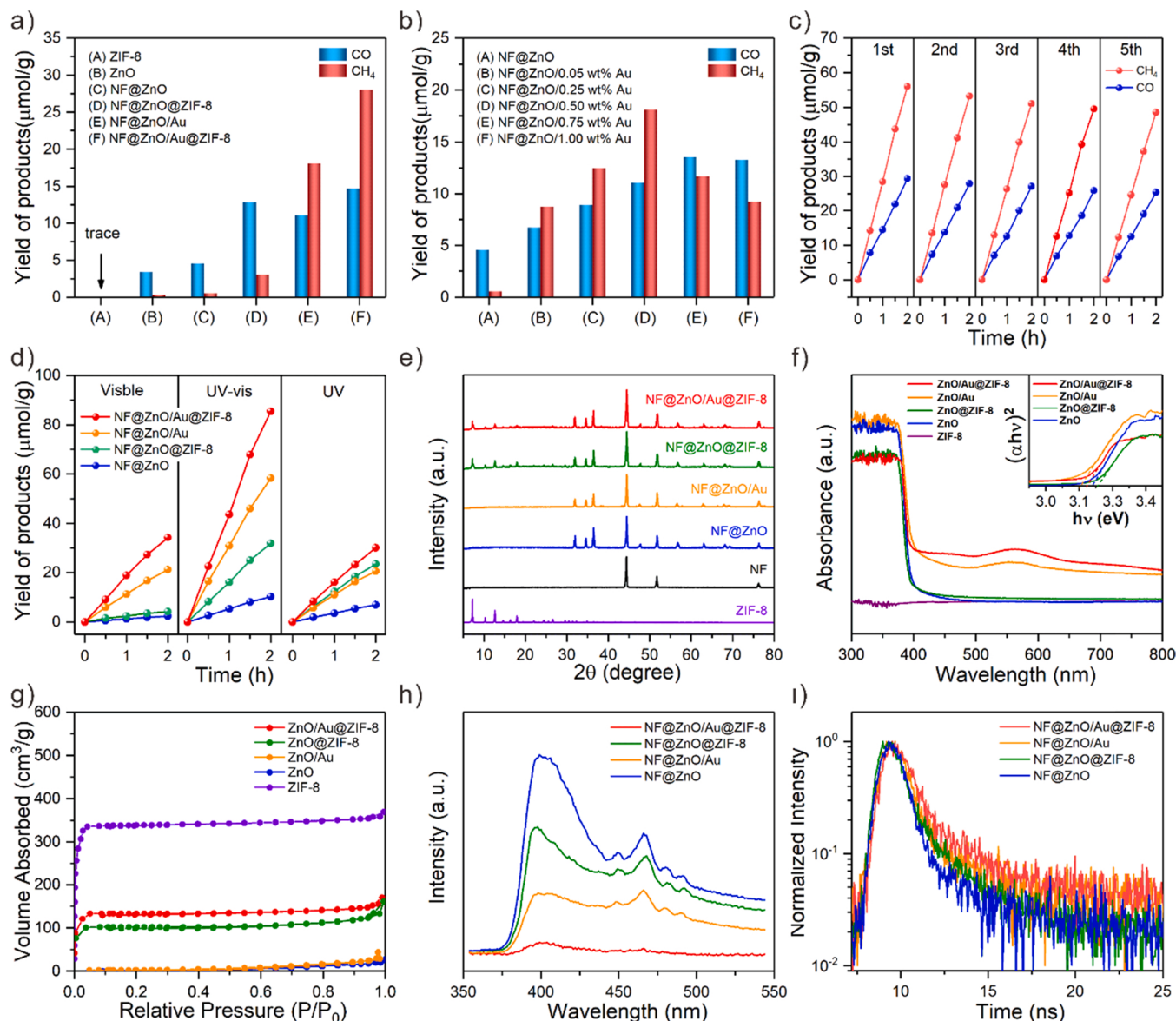


Fig. 2. Yield of products of (a) different catalysts, (b) different amounts of Au containing composites for 1 h. (c) Yield of products of NF@ZnO/Au@ZIF-8 under recycling photocatalytic production experiments. (d) Yield of products under different conditions (visible light, UV-visible light, and UV light). (e) XRD patterns. (f) UV-visible spectra. (g)  $\text{N}_2$  adsorption/desorption isotherms of different photocatalysts. (h) Steady-state PL spectra. (i) time-resolved transient PL decay spectra of catalysts.

selectivity of the product. Furthermore, when ZIF-8 layer was loaded on NF@ZnO/Au, the yield (28.01  $\mu\text{mol/g}$ ) and selectivity (60.14%) of  $\text{CH}_4$  were further improved. To study the influence of the loading amounts of Au, we observed the yield of the catalysts under different loading amount (0.05, 0.25, 0.50, 0.75, 1.0 wt%) by controlling the dosage of  $\text{HAuCl}_4$  added in the reaction system. As shown in Fig. 2b, when only Au was incorporated, the catalyst can show activity of  $\text{CH}_4$  generation. The optimal catalytic yields were 11.07  $\mu\text{mol/g}$  for CO and 17.82  $\mu\text{mol/g}$  for  $\text{CH}_4$ , and the best loading amount of Au is 0.50% in terms of mass concentration. The results indicated that in order to achieve great photocatalytic activity, it is necessary to balance the Au and ZnO exposed on the surface. Fig. 2c shows the product changes of the NF@ZnO/Au@ZIF-8 catalyst after five cycles. From the yield results of five cycles, the NF@ZnO/Au@ZIF-8 catalyst showed good stability. Improving the utilization efficiency of solar energy is a key factor of photocatalytic reaction, of which the visible light response of the semiconductor is very important. To explore the performance of photocatalysts under visible light, several catalysts were tested under visible light, ultraviolet-visible (UV-vis) light and ultraviolet (UV) light. As shown in Fig. 2d, after being loaded with Au, the response of the ZnO/Au and ZnO/Au@ZIF-8 to visible light is more obvious, showing excellent photocatalytic performance. However, ZnO and ZnO@ZIF-8 did not show obvious catalytic effect under visible light. The reason is that the SPR effect of Au makes the catalyst exhibit good photocatalytic activity under illumination.

In Fig. 2e, three characteristic XRD peaks at 44.5°, 51.9°, and 76.4° were characteristic of the (1 1 1), (2 0 0), and (2 2 0) diffraction planes of pure metallic Ni (JCPDS No. 04-0850) [35]. The typical peaks at  $2\theta = 31.8^\circ, 34.4^\circ, 36.3^\circ, 47.5^\circ, 56.6^\circ, 62.8^\circ, 66.4^\circ, 67.9^\circ, 69.1^\circ, 72.6^\circ$  and 76.9° were characteristic of the hexagonal phase wurtzite ZnO (JCPDS NO. 36-1451) [36]. In addition, the characteristic XRD peaks of ZIF-8 located at 7.4°, 16.6°, 18° and 26.6° were recorded in all samples related to ZIF-8, which were consistent with the simulation result of ZIF-8 crystal [37]. No obvious peaks of Au nanoparticle were observed in these catalysts, which may be because of its ultra-low loading (0.5%). However, the existence of Au was detected in the XPS. Fig. S2d shows the overlapped core energy level states of Au 4 f and Zn 3p. Four peaks can be assigned to Au 4  $f_{7/4}$  (83.2 eV), Au 4  $f_{5/4}$  (86.8 eV), Zn 3p<sub>3/2</sub> (88.8 eV), and Zn 3p<sub>1/2</sub> (91.8 eV) [38].

To verify the plasmon resonance effect of Au, the catalysts were tested by UV-visible diffuse reflectance spectra. As shown in Fig. 2f, ZnO/Au and ZnO/Au@ZIF-8 with Au loading have an obvious plasmon resonance peak in the range of 500–600 nm, which confirms the SPR effect of the catalyst [39]. Moreover, the absorption of ZnO/Au and ZnO/Au@ZIF-8 in the visible light band is stronger than ZnO and ZnO@ZIF-8. According to the result, the light absorption of ZIF-8 is relatively weak in the range of 300–800 nm, which also explains the poor photocatalytic effect. In addition, the band gap of each catalyst is calculated (inset in Fig. 2f). After the surface modification of Au and ZIF-8, there is no obvious change in the band gap, and all of them are around 3.20 eV. The calculated VB structures of the photocatalysts shown in Fig. S3.

To facilitate the test, except ZIF-8, the catalysts were scraped off the substrate (Ni foam) and tested for  $\text{N}_2$  adsorption/desorption isotherms. As shown in Fig. 2g, there was a strong  $\text{N}_2$  adsorption for ZnO/Au@ZIF-8 and ZnO@ZIF-8, because ZIF-8 consists of large number of micropores [40]. The measured values of  $S_{\text{BET}}$ ,  $V_p$  and  $d_p$  for all the samples were listed in Table S1. By the modification of ZIF-8, the  $S_{\text{BET}}$  of ZnO and ZnO/Au were increased from 1.98 and 2.43  $\text{m}^2/\text{g}$  to 348.2 and 406.7  $\text{m}^2/\text{g}$ , respectively.

Charge separation and transfer are essential in the efficiency of photocatalytic reduction of  $\text{CO}_2$ . The changes of surface charge dynamics of the catalysts after Au and ZIF-8 co-modification were measured by steady-state and time-resolved PL. Fig. 2h displays steady-state PL spectra of each catalyst, from which the ZnO/Au@ZIF-8 catalyst has experienced a significant quenching. The decoration of Au may

promote interfacial electron transfer effectively, because of the Schottky junction effect. In addition, the ZIF-8 modification can reduce the possibility of charge recombination due to the unique surface passivation effect. The co-modification of Au and ZIF-8 has obvious effect in suppressing recombination of carriers, resulting in the significant photoluminescence quenching of the ZnO/Au@ZIF-8 photocatalyst. The time-resolved PL decay spectra (Fig. 2i) show that the emission lifetime of ZnO/Au@ZIF-8 is much longer than that of the other samples, which is in agreement with the above steady-state PL results. By fitting the data to the calculations,  $\tau_1$ ,  $\tau_2$  and average emission lifetime ( $\tau$ ) for catalysts are listed in Table S2. The average emission lifetime ( $\tau$ ) values were 1.14, 1.62, 2.47, and 4.11 ns for ZnO, ZnO@ZIF-8, ZnO/Au, and ZnO/Au@ZIF-8 photocatalysts, respectively. The results demonstrate that the co-modification effect of Au and ZIF-8 produces significant synergistic effects in terms of reduced surface charge recombination, which effectively prolongs the lifetime of the charge carriers.

### 3.3. Relationship between selective-breathing effect and photocatalytic performance

In order to find out the most appropriate loading thickness of ZIF-8 layer and achieve the best balance of gas adsorption and desorption, we changing the reaction time for controlling the growth thickness of ZIF-8. Different NF@ZnO@ZIF-8 structures were obtained by varying the reaction time (4 h, 8 h, 12 h, 24 h, 36 h, 48 h). As shown in Fig. 3a-f, the ZIF-8 layer grew thicker with the increase of reaction time. ZIF-8 layers are evenly and continuously distributed on the surface of ZnO (Fig. 3g-h). It can be clearly seen in Fig. 3i-l that ZnO, containing the characteristic elements of Zn and O, is rod-like shape, while ZIF-8 with the characteristic elements of C and N are distributed on the outer surface of ZnO. These results exanimated that ZnO@ZIF-8 has a core-shell structure.

To achieve the best balance of gas adsorption and desorption, it is necessary to study the most suitable thickness of ZIF-8 layer. This is because, as the ZIF-8 layer becomes thicker, it may lead to the desorption of the product to be difficult, thus hindering the reaction. Fig. 3m shows the yields of CO and  $\text{CH}_4$  of the samples at different reaction times. The monolithic NF@ZnO@ZIF-8 catalyst under 24 h reaction time showed the best photocatalytic performance (CO: 12.83  $\mu\text{mol/g}$ ,  $\text{CH}_4$ : 3.06  $\mu\text{mol/g}$ ) and  $\text{CH}_4$  selectivity (17.52%). According to Fig. 3d, for the ZIF-8 layer, the best performance of the catalyst (24 h\_NF@ZnO@ZIF-8) was achieved at the best thickness of about 50 nm.

In order to explore the adsorption performance of catalysts on  $\text{CO}_2$ , we tested the adsorption capacity of each sample at room temperature by static volumetric method. As shown in the Fig. 3n, ZnO (0.018 mmol/g) and ZnO/Au (0.039 mmol/g) have very weak adsorption for  $\text{CO}_2$ . However, after loading ZIF-8 layer, ZnO@ZIF-8 (0.57 mmol/g) and ZnO/Au@ZIF-8 (0.76 mmol/g) catalysts showed strong adsorption capacity for  $\text{CO}_2$ . The adsorption capacity of ZIF-8 for  $\text{CO}_2$  also reached 1.24 mmol/g, which fully illustrates the effect of ZIF-8 in improving the ability of the catalyst to adsorb  $\text{CO}_2$ . In Fig. 3o, with the increasing ZIF-8 thickness, the  $\text{CO}_2$  adsorption capacity of the catalyst becomes stronger. Therefore, the meaning of controlling the ZIF-8 thickness is to explore the relationship between the adsorption of  $\text{CO}_2$  on the ZIF-8 layer and the yield. It has been proved that the thicker the ZIF-8 layer is, the better the  $\text{CO}_2$  adsorption effect will be. However, according to previous tests, it is found that the best photocatalytic effect is when the ZIF-8 thickness is about 50 nm (24 h\_NF@ZnO@ZIF-8). The reason may be that when the ZIF-8 thickness is greater than 50 nm, the product cannot be separated from ZIF-8 layer in time due to strong adsorption, which hinders the further progress of the reaction. To explore the adsorption selectivity of the catalyst for different gas, the catalysts were placed in different atmospheres to compare their adsorption capacity. In Fig. 3p, the adsorption capacity of ZnO/Au@ZIF-8 for different gas:  $\text{CO}_2 > \text{CO} > \text{CH}_4 > \text{N}_2$ . This shows that in the process of photocatalytic reaction, ZnO/Au@ZIF-8 will preferentially adsorb  $\text{CO}_2$ , followed by CO, and

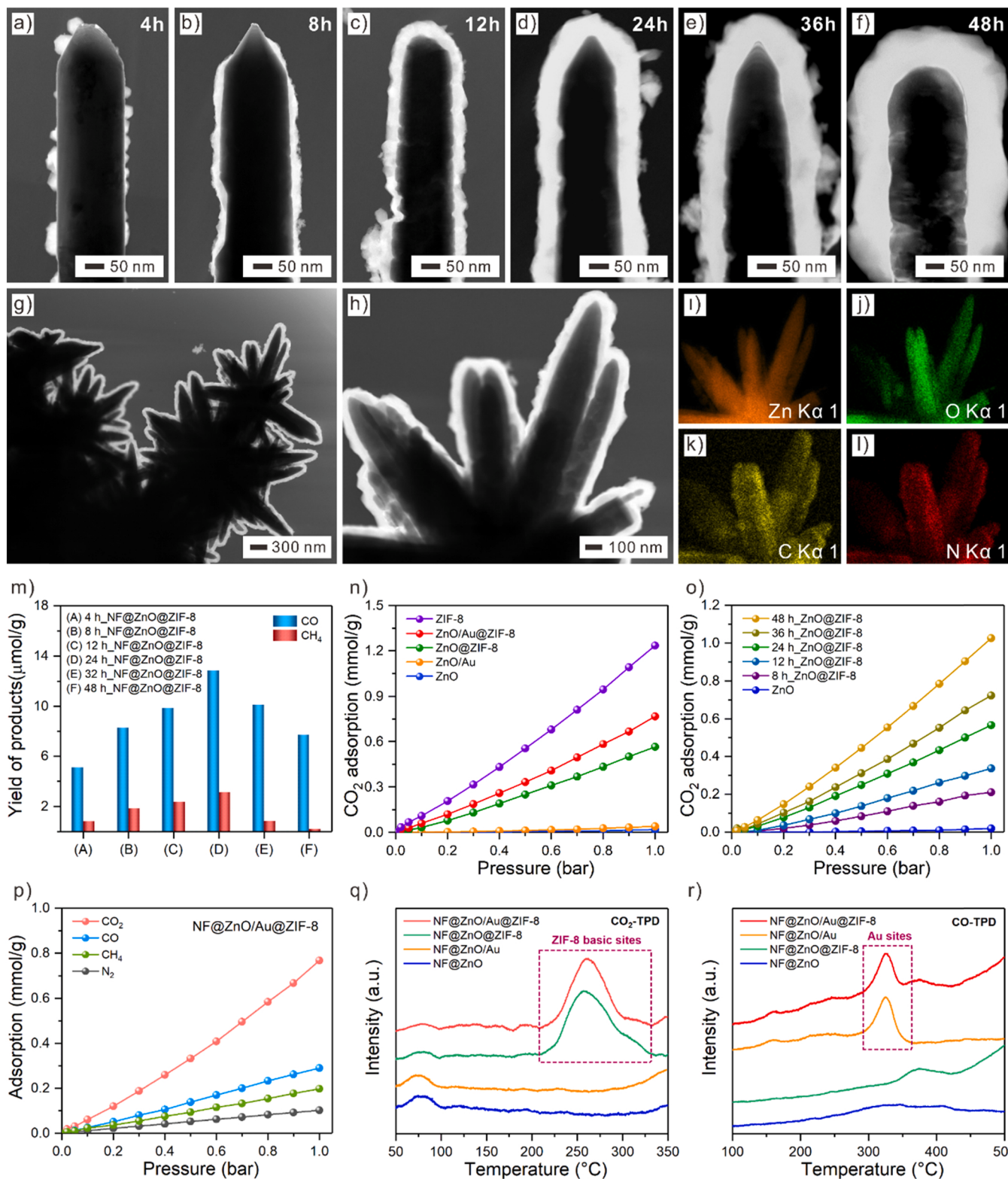


**Fig. 3.** (a-f) TEM images of NF@ZnO@ZIF-8 obtained after reaction for 4 h, 8 h, 12 h, 24 h, 36 h and 48 h, respectively. (g-h) TEM images of 24 h\_NF@ZnO@ZIF-8 catalyst. (i-o) EDS mappings of Zn, O, C and N of 24 h\_NF@ZnO@ZIF-8 catalyst. (m) Yield of products of different reaction time of NF@ZnO@ZIF-8 for 1 h under light illumination. (n-o) CO<sub>2</sub> adsorption curves of different catalysts (p) adsorption capacity of NF@ZnO/Au@ZIF-8 in different atmospheres. (q) CO<sub>2</sub>-TPD and (r) CO-TPD of different catalysts.

finally CH<sub>4</sub> and other gases. Due to the low adsorption selectivity of CH<sub>4</sub>, it cannot compete with the adsorption of CO<sub>2</sub> and CO, so it will preferentially desorb the ZIF-8 layer. And this is the selective-breathing effect of NF@ZnO/Au@ZIF-8. To verify the adsorption sites of CO<sub>2</sub> and

CO, we conducted CO<sub>2</sub>-TPD and CO-TPD experiments. As shown in the Fig. 3q, the addition of ZIF-8 caused a significant change of adsorption site. The peak located at 220–320 nm corresponds to the basic adsorption site of ZIF-8. The CO-TPD test showed that there were obvious

adsorption sites after the introduction of Au (Fig. 3r). It indicated that Au is vital in improving the selectivity of CO adsorption. Ward and co-workers used the adsorption effect of Au on CO to achieve the catalytic conversion of CO [32]. Combining previous studies on catalyst yields, it can be concluded that the adsorption of CO is crucial in the selectivity of the product.

### 3.4. Pathway and mechanism of photocatalytic $\text{CO}_2$ reduction reaction

In the in-situ FT-IR spectra (Fig. 4a), there are mainly two modes of  $\text{CO}_2$  adsorption on the NF@ZnO/Au@ZIF-8, that is, m- $\text{CO}_3^{2-}$  (1310, 1384, 1450 and 1510  $\text{cm}^{-1}$ ) and b- $\text{CO}_3^{2-}$  (1335 and 1584  $\text{cm}^{-1}$ ) [41–44]. The peaks located at 1097, 1240 and 1440  $\text{cm}^{-1}$  can be ascribed to  $\text{HCO}_3^-$ , which is an important intermediate for reducing CO [42,44,45]. In addition, the formation of some important intermediates, such as CHO (1025  $\text{cm}^{-1}$ ), - $\text{CH}_2\text{O}$  (1180 and 1460  $\text{cm}^{-1}$ ) and - $\text{OCH}_3$  (1150 and 1432  $\text{cm}^{-1}$ ), confirmed the photocatalytic conversion of  $\text{CO}_2$  to  $\text{CH}_4$  [45,46]. The sources of CO and  $\text{CH}_4$  produced were essential to photocatalytic reaction. In Fig. 4b, we carried out GC-MS analysis of the products generated from the  $^{13}\text{CO}_2$  isotope experiments and determined that the carbon source of the product comes from reactant ( $\text{CO}_2$ ) rather than the decomposition of the catalysts. The main signals at  $m/z = 17$  and 29 in GC-MS could be assigned to  $^{13}\text{CH}_4$  and  $^{13}\text{CO}$ , respectively. After determining the carbon source and intermediates of the product, a possible photocatalytic formation pathway for the evolution of CO and  $\text{CH}_4$  on the surface of NF@ZnO/Au@ZIF-8 can be drawn. As shown in Fig. 4c, according to the detected  $\text{CO}_2$  adsorption mode, there are mainly two types, m- $\text{CO}_3^{2-}$  and b- $\text{CO}_3^{2-}$ . Subsequently, the m- $\text{CO}_3^{2-}$  and b- $\text{CO}_3^{2-}$  react with protons and photogenerated electrons to form  $\text{HCO}_3^-$ . Afterwards, the  $\text{HCO}_3^-$  further obtains protons and photogenerated electrons to form CO intermediate. These CO are easy to release and difficult to reduce further. This is why the main product of ZnO, NF@ZnO, and NF@ZnO@ZIF-8 are all CO. However, after introducing Au into the catalyst, CO is further converted on the surface of the catalyst due to adsorption of CO on Au. CO<sub>2</sub> can be further reduced to -CHO because of the high surface electron density of gold. Then -CHO gained protons and photogenerated electrons to form - $\text{CH}_2\text{O}$ . Afterwards, the - $\text{CH}_2\text{O}$  further obtains protons and photogenerated electrons to form - $\text{OCH}_3$ . Finally, the - $\text{OCH}_3$  reacts with protons and photogenerated electrons to  $\text{CH}_4$ .

In general, a preliminary mechanism for photocatalytic conversion of  $\text{CO}_2$  in NF@ZnO/Au@ZIF-8 photocatalysts is proposed (Fig. 4d). Electrons are generated in the conduction band of ZnO under UV-vis excitation. One part of the electrons is used for the conversion of  $\text{CO}_2$  to CO, since  $\text{CO}_2$  is probably adsorbed on ZnO for reduction from the previous in situ FT-IR analysis. Another part of electrons transferred to Au NP by the Schottky barrier, which ensures the photogenerated carriers separated effectively. [47] Meanwhile, the SPR effect of Au further promotes the generation and aggregation of charges. According to the previous adsorption test and in-situ IR test, it is proved that the reduction of CO on Au is feasible, so the electrons on Au probably participate in the transversion of CO to  $\text{CH}_4$ . Moreover, under visible light, photogenerated electrons from Au plasma excitation can migrate into the conduction band of ZnO due to the shift of the Au Fermi energy level to a more negative potential, which facilitates the conversion of  $\text{CO}_2$  to products [48–50]. In addition, the holes left in the valence band of ZnO oxidize  $\text{H}_2\text{O}$  to generate  $\text{O}_2$  and  $\text{H}^+$ . In summary, the reduction of  $\text{CO}_2$  is divided into two steps: the first step is to reduce  $\text{CO}_2$  to CO on the surface of ZnO and the second step is to reduce CO to  $\text{CH}_4$  on the surface of Au. Au loading on ZnO is not only beneficial to the separation of photogenerated carriers, but also boosts the generation of hot electrons to have participation in the conversion of  $\text{CO}_2$ , which can also enhance the adsorption of visible light. It can effectively adsorb and reduce CO and further drive the reaction. The high electron density on the surface of Au significantly improves the photocatalytic efficiency of  $\text{CO}_2$  reduction, especially because the formation of  $\text{CH}_4$  requires more active electrons. As illustrated in Fig. 4e, we used the schematic diagram of  $\text{CO}_2$

conversion of the gas flow and conversion path to simulate the selective breathing process of NF@ZnO/Au@ZIF-8. The selective adsorption and desorption process of gas is divided into three main steps. The first step is that ZIF-8 adsorb a large amount of  $\text{CO}_2$ , which leads to the reduction of  $\text{CO}_2$  to CO on the surface of ZnO. The second step is to convert CO to  $\text{CH}_4$  by Au through the adsorbing CO generated in the previous step. The third step is that  $\text{CH}_4$  escapes from ZIF-8, because its adsorption selectivity is low and it cannot compete with the adsorption of  $\text{CO}_2$  and CO. The cycle of these three steps produced the unique selective-breathing properties of the monolithic NF@ZnO/Au@ZIF-8 catalyst, which consistently and efficiently drove the reaction.

### 3.5. Enhancement of photocatalytic $\text{CO}_2$ reduction process by the photo-thermal-magnetic coupling

Because of the discontinuity and low efficiency of solar energy, we put the monolithic catalyst under the photo-thermal-magnetic coupling for the photocatalytic reaction. The yield and selectivity of catalysts under photo-thermal-magnetic coupling reaction system are summarized in Table S5–S7. Fig. 5a shows yields of NF@ZnO/Au@ZIF-8 catalyst under different conditions. In the dark, there is almost no yield (AMF/NAMF) no matter whether an alternating magnetic field is introduced or not. It indicates that only relying on the magnetic field cannot reach the reaction temperature of the thermal catalysis of  $\text{CO}_2$  conversion. The main catalytic form of the product still comes from photocatalysis, while the thermal field and magnetic field are used to assist in improving the photocatalysis efficiency. Under NAMF light conditions, the yields of CO and  $\text{CH}_4$  with NF@ZnO/Au@ZIF-8 were only 14.67 and 28.01  $\mu\text{mol/g}$ . However, under the combined condition of illumination and magnetic field (AMF light), the yields of CO and  $\text{CH}_4$  were elevated to 21.36 and 270.12  $\mu\text{mol/g}$ , which was nearly ten times. As shown in Fig. 5b, in the case of AMF light, the other catalysts also showed a significant increase in yield except for ZIF-8 and ZnO. This demonstrates that magnetic fields improve the photocatalytic efficiency with a certain range. Moreover, NF-based catalysts showed significant yield enhancement in magnetic fields. This is because the NF-based catalyst can better sense the magnetic field heat. In addition, the support of the fixed skeleton avoided the problems of powder agglomeration and uneven heating. In photo-thermal-magnetic coupling reaction systems, it is extremely important to determine the temperature of the reaction system and its influence. The infrared real-time temperature measuring device used in the photocatalytic reaction is shown in Fig. S4. In Fig. 5c, the temperature of each reaction system was tested for different situations. Only under illumination, the reaction temperature is only about 70 °C. However, under AMF illumination, the surface temperature of NF@ZnO/Au@ZIF-8 can attain about 180 °C at the highest. Most of this heat comes from the magneto-thermal effect, as the temperature can reach about 160 °C under AMF dark condition. The photo-thermal-magnetic coupling reaction system further accelerates the reaction process by using the photothermal and magnetothermal system. Furthermore, in Fig. S5, the decomposition temperature of ZIF-8 is shown to be much higher than the temperature of the reaction system based on the TGA curve. This confirms the carbon source of the product and the stability of the catalyst under the reaction system. In Fig. 5d, the test results under NAMF light and NAMF dark conditions showed an increase in photocurrent density of 5.23  $\text{mA}/\text{cm}^2$  for the same bias voltage (−1.5 V vs. SCE), which indicated a better photoresponse performance of the NF@ZnO/Au@ZIF-8 catalyst. A comparison of the test results under NAMF light and AMF light conditions showed the photocurrent density increased by 12.57  $\text{mA}/\text{cm}^2$  at the same bias voltage (−1.5 V vs. SCE), which is mainly due to the coupled magnetic field that promotes charge separation on the surface of catalyst [51]. Fig. 5e shows the transient photocurrent response of NF@ZnO/Au@ZIF-8 under different conditions. When the magnetic field was introduced, the maximum photocurrent density of AMF condition (1.164  $\text{mA}/\text{cm}^2$ ) was nearly twice that of NAMF condition (0.584  $\text{mA}/\text{cm}^2$ ). This means that

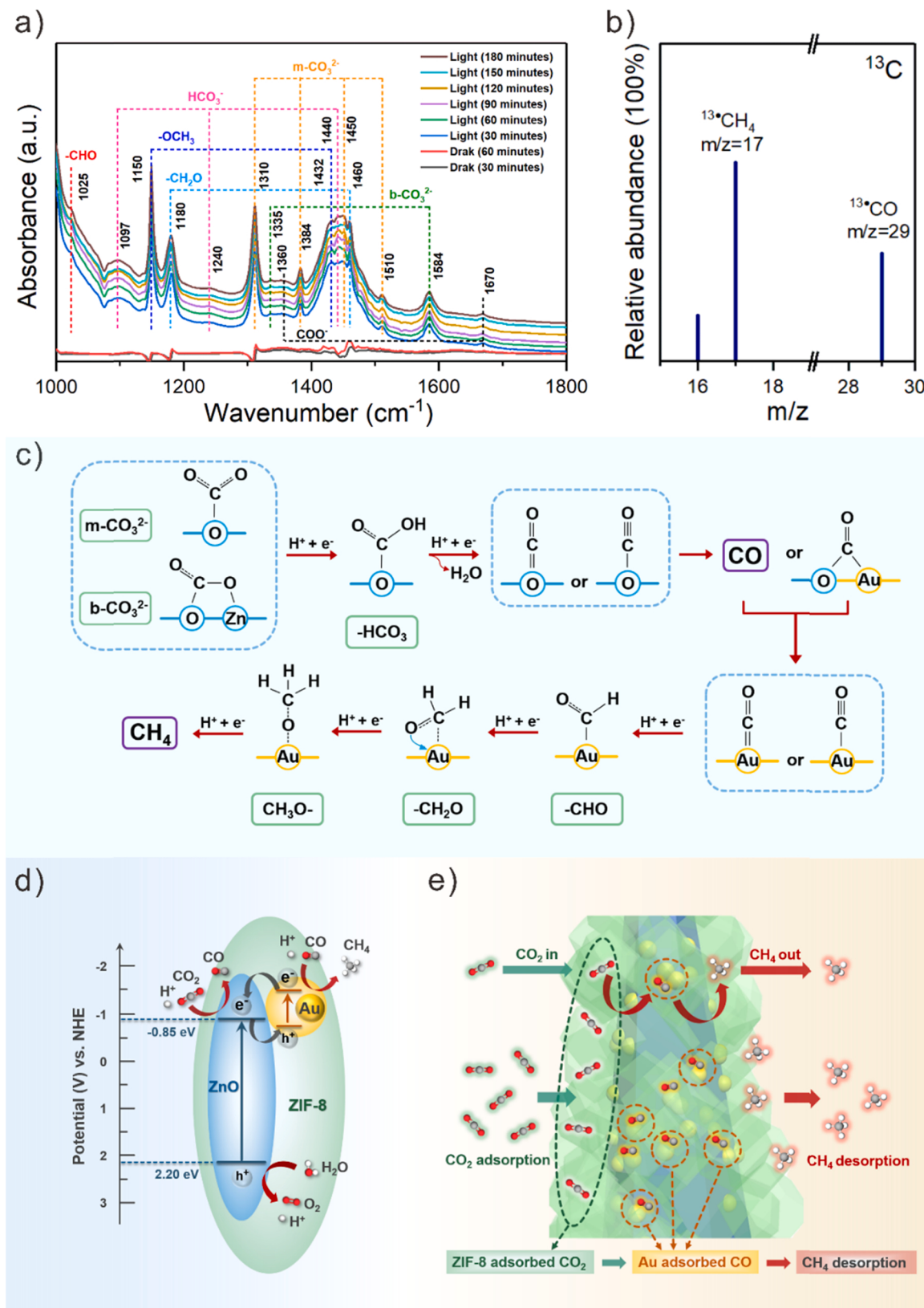


**Fig. 4.** (a) In situ FT-IR spectra of NF@ZnO/Au@ZIF-8 in a flow of a  $\text{CO}_2/\text{H}_2\text{O}$  vapor mixture under dark condition (0–60 min) and under illumination (180 min). (b) GC-MS analysis of the products generated from the  $^{13}\text{CO}_2$  isotope experiments of NF@ZnO/Au@ZIF-8. (c) A possible formation pathway for the evolution of CO and  $\text{CH}_4$  on the surface of NF@ZnO/Au@ZIF-8. (d) Illustration of the band structure and charge transfer process of NF@ZnO/Au@ZIF-8 catalyst under UV-vis light. (e) Schematic diagram of  $\text{CO}_2$  photocatalytic reduction promoted by selective breathing of NF@ZnO/Au@ZIF-8 catalyst.

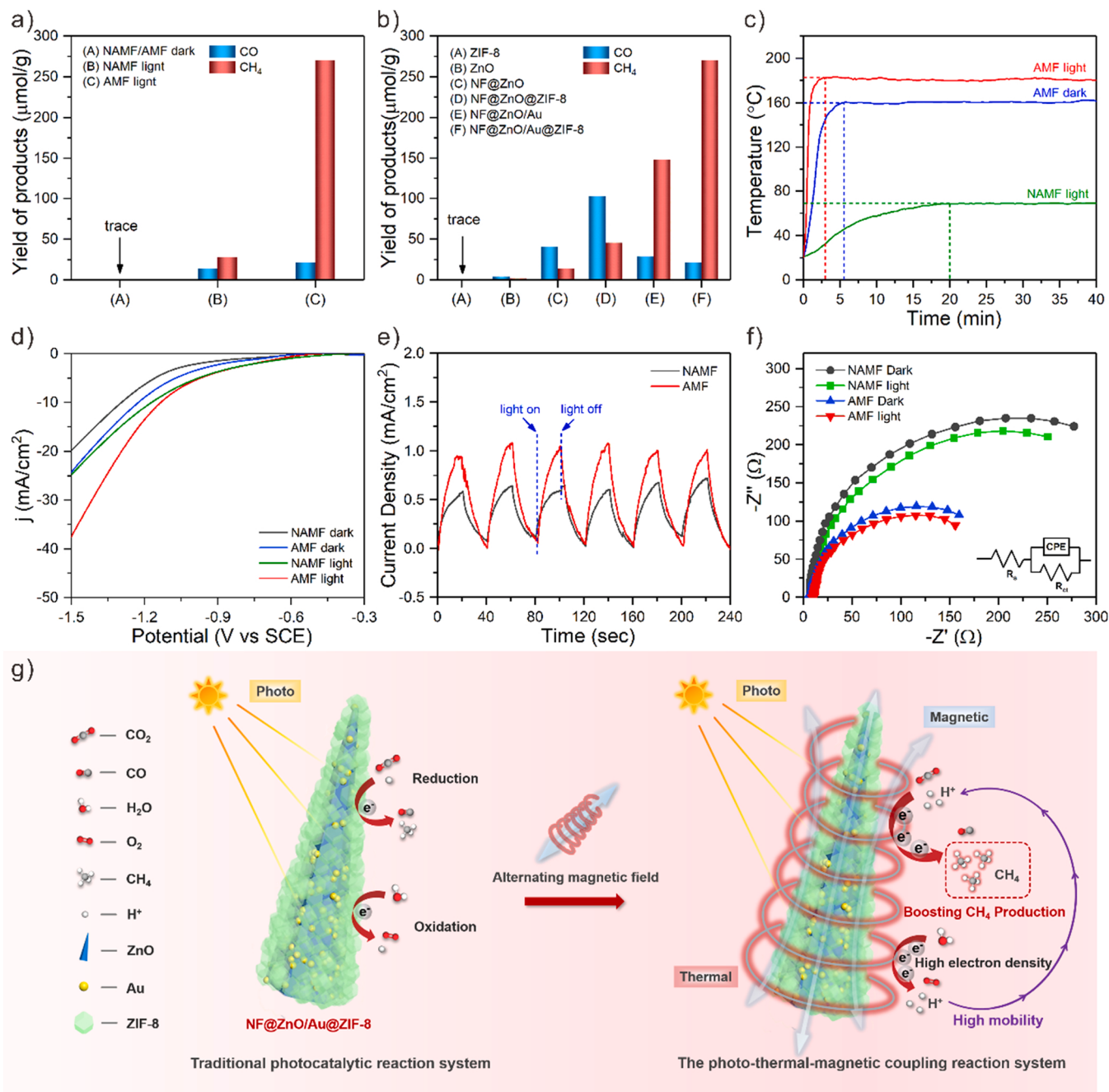


**Fig. 5.** Yield of products of (a) NF@ZnO/Au@ZIF-8 under different conditions, (b) different catalysts under AMF and light illumination for 1 h. (c) the temperature of NF@ZnO/Au@ZIF-8 surface under three different conditions. (d) transient photocurrent response under different conditions. (e) Linear sweep voltammograms (LSV) of NF@ZnO/Au@ZIF-8 under different conditions. (f) EIS Nyquist plots of NF@ZnO/Au@ZIF-8 under different conditions. (g) Schematic diagram of enhanced CO<sub>2</sub> reduction process by the photo-thermal-magnetic coupling reaction system.

under the magnetic field, the photogenerated carrier density will increase, which is more favorable to the photocatalytic reduction of CO<sub>2</sub>. The electrochemical impedance spectroscopy (EIS) Nyquist plots further illustrated the effect of alternating magnetic field on the carriers. As shown in Fig. 5f, EIS Nyquist plots of NF@ZnO/Au@ZIF-8 catalyst was carried out under four different conditions. The charge transfer resistances (R<sub>ct</sub>) and solution resistances (R<sub>s</sub>) are summarized in Table S3. There is a small decrease in the arc diameter (R<sub>ct</sub>) in the Nyquist plot after illumination, both in NAMF and AMF conditions. The decrease of R<sub>ct</sub> is due to the photoconductive effect. This phenomenon is not obvious because the catalyst contains conductive metals (NF), resulting in low total resistance of the catalyst. Notably, whether there

was light or not, under the effect of magnetic field, the value of R<sub>ct</sub> will be significantly decreased. This phenomenon illustrates that the magnetic field can reduce the charge transfer resistance of photocatalyst, thus greatly improving the charge transfer efficiency of the interface.

At last, a summary of the photo-thermal-magnetic coupling reaction system is presented. As shown in Fig. 5g, combined with the analysis of previous tests, the coupled magnetic field can increase the photogenerated carrier density on the catalyst surface, increase the photogenerated carrier migration rate and decrease the photogenerated carrier complexation. These advantages offer the possibility to improve the efficiency of CO<sub>2</sub> photocatalytic conversion and the high selectivity of CH<sub>4</sub>. In addition, the thermal field generated by the magnetic field

and light also contributes to the CO<sub>2</sub> photocatalytic reaction system. The function of the thermal field is to mainly accelerate the reaction rate, enhance the selectivity of CH<sub>4</sub>, and accelerate the gas phase flow, thus driving the reaction process. Moreover, most of the heat in the thermal field is provided by the magnetic field, which also indicates the importance of introducing the magnetic field into the system.

#### 4. Conclusions

As a consequence, we demonstrated a new construction of selective-breathing monolithic NF@ZnO/Au@ZIF-8 catalyst to promote the efficient conversion of CO<sub>2</sub> to CH<sub>4</sub> by photo-thermal-magnetic coupling. The selective-breathing monolithic NF@ZnO/Au@ZIF-8 catalyst has good selective adsorption performance of CO<sub>2</sub> (0.79 mmol/g) and CO (0.30 mmol/g), long photogenerated carrier lifetime (4.11 ns), and good visible light absorption efficiency. Under the illumination condition, the yields of CO and CH<sub>4</sub> of selective-breathing monolithic NF@ZnO/Au@ZIF-8 photocatalyst can reach 14.67 and 28.01 μmol/g, respectively, and the selectivity of CH<sub>4</sub> can achieve 61.2%. Upon photo-thermal-magnetic coupling, the yield of CH<sub>4</sub> of the selective-breathing monolithic NF@ZnO/Au@ZIF-8 photocatalyst can be significantly increased to nearly 10 times (270.02 μmol/g) and the selectivity of CH<sub>4</sub> can be improved to 89.72%. By the photo-thermal-magnetic coupling, the monolithic NF@ZnO/Au@ZIF-8 photocatalyst can significantly increase the reaction temperature (about 180 °C), greatly increase the photocurrent density (1.164 mA/cm<sup>2</sup>), and reduce the arc diameter (113 Ω), prompting faster migration of charge carriers to the surface reaction sites and more carriers per unit time to participate in the surface reaction. The new strategy proposed in this paper not only designs photocatalysts with higher reaction efficiency and more practical applications from the perspective of the reaction gas adsorption and desorption process, but also suggests new possibilities for future photocatalytic applications in a photo-thermal-magnetic coupled reaction system.

#### CRediT authorship contribution statement

**Zhu Tang:** Data curation, Formal analysis, Investigation, Writing – original draft. **Fengfan Zhu:** Writing – review & Editing, Visualization. **Jiancheng Zhou:** Validation, Writing – review & editing, Supervision, Funding acquisition. **Wenshuai Chen:** Conceptualization, Writing – review & editing, Supervision, Funding acquisition. **Ke Wang:** Formal analysis, Validation. **Maochang Liu:** Conceptualization, Writing – review & editing, Supervision, Funding acquisition. **Nan Wang:** Project administration, Validation. **Naixu Li:** Conceptualization, Writing – review & editing, Funding acquisition.

#### Declaration of Competing Interest

The authors declare that they have no known competing financial interests or personal relationships that could have appeared to influence the work reported in this paper.

#### Acknowledgments

This work was financially supported by the National Natural Science Foundation of China (Nos. 22078057, 21576050 and 51602052), Fundamental Research Funds for the Central Universities of China (No. 3207045403, 3207045409, 3207046414), Foundation of Jiangsu Key Laboratory for Biomass Energy and Material (JSBEM202001), Priority Academic Program Development of Jiangsu Higher Education Institutions (PAPD), Zhongying Young Scholars of Southeast University, Applied Basic Research Program of Suzhou (SYG202026), Postgraduate Research & Practice Innovation Program of Jiangsu Province (SJCX20\_0014, SJCX20\_0015), and Innovation Platform Project Supported by Jiangsu Province of China (6907041203).

#### Appendix A. Supporting information

Supplementary data associated with this article can be found in the online version at doi:10.1016/j.apcatb.2022.121267.

#### References

- [1] K. Li, B. Peng, T. Peng, Recent advances in heterogeneous photocatalytic CO<sub>2</sub> conversion to solar fuels, *ACS Catal.* 6 (2016) 7485–7527, <https://doi.org/10.1021/acscatal.6b02089>.
- [2] D. Chen, H. Zhu, S. Yang, N. Li, Q. Xu, H. Li, J. He, J. Lu, Micro-nanocomposites in environmental management, *Adv. Mater.* 28 (2016) 10443–10458, <https://doi.org/10.1002/adma.201601486>.
- [3] S. Wang, Y. Zhang, T. Zhang, F. Dong, H. Huang, Readily attainable spongy foam photocatalyst for promising practical photocatalysis, *Appl. Catal. B Environ.* 208 (2017) 75–81, <https://doi.org/10.1016/j.apcatb.2017.02.033>.
- [4] C. Zhang, H.C. Yang, L.S. Wan, H.Q. Liang, H. Li, Z.K. Xu, Polydopamine-coated porous substrates as a platform for mineralized beta-FeOOH nanorods with photocatalysis under sunlight, *ACS Appl. Mater. Interfaces* 7 (2015) 11567–11574, <https://doi.org/10.1021/acsmi.5b02530>.
- [5] H. Zhu, D. Chen, N. Li, Q. Xu, H. Li, J. He, J. Lu, Dual-layer copper mesh for integrated oil-Water separation and water purification, *Appl. Catal. B Environ.* 200 (2017) 594–600, <https://doi.org/10.1016/j.apcatb.2016.07.028>.
- [6] Y. Li, W. Cui, L. Liu, R. Zong, W. Yao, Y. Liang, Y. Zhu, Removal of Cr(VI) by 3D TiO<sub>2</sub>–graphene hydrogel via adsorption enriched with photocatalytic reduction, *Appl. Catal. B Environ.* 199 (2016) 412–423, <https://doi.org/10.1016/j.apcatb.2016.06.053>.
- [7] M. Zhang, W. Luo, Z. Wei, W. Jiang, D. Liu, Y. Zhu, Separation free C<sub>3</sub>N<sub>4</sub>/SiO<sub>2</sub> hybrid hydrogels as high active photocatalysts for TOC removal, *Appl. Catal. B Environ.* 194 (2016) 105–110, <https://doi.org/10.1016/j.apcatb.2016.04.049>.
- [8] J. Blanco, P. Avila, A. Bahamonde, E. Alvarez, B. Sánchez, M. Romero, Photocatalytic destruction of toluene and xylene at gas phase on a titania based monolithic catalyst, *Catal. Today* 29 (1996) 437–442, [https://doi.org/10.1016/0920-5861\(95\)00317-7](https://doi.org/10.1016/0920-5861(95)00317-7).
- [9] J. Yi, L. Huang, H. Wang, H. Yu, F. Peng, AgI/TiO<sub>2</sub> nanobelts monolithic catalyst with enhanced visible light photocatalytic activity, *J. Hazard Mater.* 284 (2015) 207–214, <https://doi.org/10.1016/j.jhazmat.2014.11.020>.
- [10] Z. Liu, F. Wang, Z. Zhang, S. Min, Interfacing CdS particles on Ni foam as a three-dimensional monolithic photocatalyst for efficient visible-light-driven H<sub>2</sub> evolution, *Int. J. Hydrog. Energy* 45 (2020) 31678–31688, <https://doi.org/10.1016/j.ijhydene.2020.09.031>.
- [11] L. Hu, G. Zhang, M. Liu, Q. Wang, S. Dong, P. Wang, Application of nickel foam-supported Co<sub>3</sub>O<sub>4</sub>–Bi<sub>2</sub>O<sub>3</sub> as a heterogeneous catalyst for BPA removal by peroxymonosulfate activation, *Sci. Total Environ.* 647 (2019) 352–361, <https://doi.org/10.1016/j.scitotenv.2018.08.003>.
- [12] X. Li, S. Liu, K. Fan, Z. Liu, B. Song, J. Yu, MOF-based transparent passivation layer modified ZnO nanorod arrays for enhanced photo-electrochemical water splitting, *Adv. Energy Mater.* 8 (2018), 1800101, <https://doi.org/10.1002/aenm.201800101>.
- [13] Y. Zhang, L. Liu, B. Van der Bruggen, M.K.H. Leung, F. Yang, A free-standing 3D nano-composite photo-electrode—Ag/ZnO nanorods arrays on Ni foam effectively degrade berberine, *Chem. Eng. J.* 373 (2019) 179–191, <https://doi.org/10.1016/j.cej.2019.05.026>.
- [14] Y. Xi, Y. Zhang, X. Cai, Z. Fan, K. Wang, W. Dong, Y. Shen, S. Zhong, L. Yang, S. Bai, Pt/Cu thickness-modulated interfacial charge transfer and surface reactivity in stacked graphene/Pd@PtCu heterostructures for highly efficient visible-light reduction of CO<sub>2</sub> to CH<sub>4</sub>, *Appl. Catal. B Environ.* 305 (2022), 121069, <https://doi.org/10.1016/j.apcatb.2022.121069>.
- [15] F. Liao, Y. Huang, J. Ge, W. Zheng, K. Tedsree, P. Collier, X. Hong, S.C. Tsang, Morphology-dependent interactions of ZnO with Cu nanoparticles at the materials' interface in selective hydrogenation of CO<sub>2</sub> to CH<sub>3</sub>OH, *Angew. Chem. Int. Ed. Engl.* 50 (2011) 2162–2165, <https://doi.org/10.1002/ange.201007108>.
- [16] W. Jiang, J. Low, K. Mao, D. Duan, S. Chen, W. Liu, C.W. Pao, J. Ma, S. Sang, C. Shu, X. Zhan, Z. Qi, H. Zhang, Z. Liu, X. Wu, R. Long, L. Song, Y. Xiong, Pd-Modified ZnO–Au enabling alkoxy intermediates formation and dehydrogenation for photocatalytic conversion of methane to ethylene, *J. Am. Chem. Soc.* 143 (2021) 269–278, <https://doi.org/10.1021/jacs.0c10369>.
- [17] Q. Deng, X. Duan, D.H. Ng, H. Tang, Y. Yang, M. Kong, Z. Wu, W. Cai, G. Wang, Ag nanoparticle decorated nanoporous ZnO microrods and their enhanced photocatalytic activities, *ACS Appl. Mater. Interfaces* 4 (2012) 6030–6037, <https://doi.org/10.1021/am301682g>.
- [18] S. Zhong, Y. Xi, S. Wu, Q. Liu, L. Zhao, S. Bai, Hybrid cocatalysts in semiconductor-based photocatalysis and photoelectrocatalysis, *J. Mater. Chem. A* 8 (2020) 14863–14894, <https://doi.org/10.1039/d0ta04977h>.
- [19] C. Wang, O. Ranasingha, S. Natesakhawat, P.R. Ohodnicki Jr., M. Andio, J. P. Lewis, C. Matranga, Visible light plasmonic heating of Au-ZnO for the catalytic reduction of CO<sub>2</sub>, *Nanoscale* 5 (2013) 6968–6974, <https://doi.org/10.1039/c3nr02001k>.
- [20] T. Ward, L. Delannoy, R. Hahn, S. Kendell, C.J. Pursell, C. Louis, B.D. Chandler, Effects of Pd on catalysis by Au: CO adsorption, CO oxidation, and cyclohexene hydrogenation by supported Au and Pd–Au Catalysts, *ACS Catal.* 3 (2013) 2644–2653, <https://doi.org/10.1021/cs400569v>.

[21] Y. Su, H. Xu, J. Wang, X. Luo, Z.-l Xu, K. Wang, W. Wang, Nanorattle Au@PtAg encapsulated in ZIF-8 for enhancing CO<sub>2</sub> photoreduction to CO, *Nano Res.* 12 (2018) 625–630, <https://doi.org/10.1007/s12274-018-2269-4>.

[22] N.A.H.Md Nordin, A.F. Ismail, A. Mustafa, R.S. Murali, T. Matsuura, Utilizing low ZIF-8 loading for an asymmetric PSf/ZIF-8 mixed matrix membrane for CO<sub>2</sub>/CH<sub>4</sub> separation, *RSC Adv.* 5 (2015) 30206–30215, <https://doi.org/10.1039/C5RA00567A>.

[23] C. Song, Z. Wang, Z. Yin, D. Xiao, D. Ma, Principles and applications of photothermal catalysis, *Chem. Catal.* 2 (2022) 52–83, <https://doi.org/10.1016/j.chechat.2021.10.005>.

[24] X. Wang, W. Gao, Z. Zhao, L. Zhao, J.P. Claverie, X. Zhang, J. Wang, H. Liu, Y. Sang, Efficient photo-electrochemical water splitting based on hematite nanorods doped with phosphorus, *Appl. Catal. B Environ.* 248 (2019) 388–393, <https://doi.org/10.1016/j.apcatb.2019.02.048>.

[25] L. Wang, S. Liu, Z. Wang, Y. Zhou, Y. Qin, Z.L. Wang, Piezotronic effect enhanced photocatalysis in strained anisotropic ZnO/TiO<sub>2</sub> nanoplatelets via thermal stress, *ACS Nano* 10 (2016) 2636–2643, <https://doi.org/10.1021/acsnano.5b07678>.

[26] H. Li, Y. Sang, S. Chang, X. Huang, Y. Zhang, R. Yang, H. Jiang, H. Liu, Z.L. Wang, Enhanced ferroelectric-nanocrystal-based hybrid photocatalysis by ultrasonic-wave-generated piezophototronic effect, *Nano Lett.* 15 (2015) 2372–2379, <https://doi.org/10.1021/nl504630j>.

[27] Z. Ai, P. Yang, X. Lu, Degradation of 4-chlorophenol by a microwave assisted photocatalysis method, *J. Hazard Mater.* 124 (2005) 147–152, <https://doi.org/10.1016/j.jhazmat.2005.04.027>.

[28] W. Hou, S.B. Cronin, A review of surface plasmon resonance-enhanced photocatalysis, *Adv. Funct. Mater.* 23 (2013) 1612–1619, <https://doi.org/10.1002/adfm.201202148>.

[29] J. Zhu, M. Chen, H. Wei, N. Yerra, N. Haldolaarachchige, Z. Luo, D.P. Young, T. C. Ho, S. Wei, Z. Guo, Magnetocapacitance in magnetic microtubular carbon nanocomposites under external magnetic field, *Nano Energy* 6 (2014) 180–192, <https://doi.org/10.1016/j.nanoen.2014.04.002>.

[30] J. Li, Q. Pei, R. Wang, Y. Zhou, Z. Zhang, Q. Cao, D. Wang, W. Mi, Y. Du, Enhanced photocatalytic performance through magnetic field boosting carrier transport, *ACS Nano* 12 (2018) 3351–3359, <https://doi.org/10.1021/acsnano.7b08770>.

[31] M. Ghoussoub, M. Xia, P.N. Duchesne, D. Segal, G. Ozin, Principles of photothermal gas-phase heterogeneous CO<sub>2</sub> catalysis, *Energy Environ. Sci.* 12 (2019) 1122–1142, <https://doi.org/10.1039/C8EE02790K>.

[32] N. Li, Y. Tu, K. Wang, D. Huang, Q. Shen, W. Chen, J. Zhou, Q. Ma, M. Liu, Construction of a Photo-thermal-magnetic coupling reaction system for enhanced CO<sub>2</sub> reduction to CH<sub>4</sub>, *Chem. Eng. J.* 421 (2021), 129940, <https://doi.org/10.1016/j.cej.2021.129940>.

[33] Y. Tian, T. Tatsuma, Mechanisms and applications of plasmon-induced charge separation at TiO<sub>2</sub> films loaded with gold nanoparticles, *J. Am. Chem. Soc.* 127 (2004) 7632–7637, <https://doi.org/10.1021/ja042192u>.

[34] M. Xiao, J. Zhu, L. Ma, Z. Jin, J. Ge, X. Deng, Y. Hou, Q. He, J. Li, Q. Jia, S. Mukerjee, R. Yang, Z. Jiang, D. Su, C. Liu, W. Xing, Microporous framework induced synthesis of single-atom dispersed Fe-N-C Acidic ORR catalyst and its in situ reduced Fe-N<sub>4</sub> active site identification revealed by X-ray absorption spectroscopy, *ACS Catal.* 8 (2018) 2824–2832, <https://doi.org/10.1021/acscatal.8b00138>.

[35] J.-j Ruan, Y.-q Huo, B. Hu, Three-dimensional Ni(OH)<sub>2</sub>/Cu<sub>2</sub>O/CuO porous cluster grown on nickel foam for high performance supercapacitor, *Electrochim. Acta* 215 (2016) 108–113, <https://doi.org/10.1016/j.electacta.2016.08.064>.

[36] Y.J. Jang, J.-W. Jang, J. Lee, J.H. Kim, H. Kumagai, J. Lee, T. Minegishi, J. Kubota, K. Domen, J.S. Lee, Selective CO production by Au coupled ZnTe/ZnO in the photoelectrochemical CO<sub>2</sub> reduction system, *Energy Environ. Sci.* 8 (2015) 3597–3604, <https://doi.org/10.1039/C5EE01445J>.

[37] Q. Liu, Z.-X. Low, L. Li, A. Razmjou, K. Wang, J. Yao, H. Wang, ZIF-8/Zn<sub>2</sub>GeO<sub>4</sub> nanorods with an enhanced CO<sub>2</sub> adsorption property in an aqueous medium for photocatalytic synthesis of liquid fuel, *J. Mater. Chem. A* 1 (2013) 11563–11569, <https://doi.org/10.1039/C3TA12433A>.

[38] X. Xue, L. Chen, C. Wang, Y. Qiao, C. Zhao, H. Wang, P. Nie, J. Li, J. Zhao, L. Chang, Controlled synthesis of a PS/Au/ZIF-8 hybrid structure as a SERS substrate for ultrasensitive detection, *N. J. Chem.* 45 (2021) 1355–1362, <https://doi.org/10.1039/DONJ05400C>.

[39] S.S. Rayalu, D. Jose, M.V. Joshi, P.A. Mangrulkar, K. Shrestha, K. Klabunde, Photocatalytic water splitting on Au/TiO<sub>2</sub> nanocomposites synthesized through various routes: enhancement in photocatalytic activity due to SPR effect, *Appl. Catal. B Environ.* 142–143 (2013) 684–693, <https://doi.org/10.1016/j.apcatb.2013.05.057>.

[40] X. Wang, J. Liu, S. Leong, X. Lin, J. Wei, B. Kong, Y. Xu, Z.X. Low, J. Yao, H. Wang, Rapid Construction of ZnO@ZIF-8 heterostructures with size-selective photocatalysis properties, *ACS Appl. Mater. Interfaces* 8 (2016) 9080–9087, <https://doi.org/10.1021/acsmami.6b00028>.

[41] F. Xu, K. Meng, B. Zhu, H. Liu, J. Xu, J. Yu, Graphdiyne: a new photocatalytic CO<sub>2</sub> reduction cocatalyst, *Adv. Funct. Mater.* 29 (2019), 1904256, <https://doi.org/10.1002/adfm.201904256>.

[42] Y. He, H. Rao, K. Song, J. Li, Y. Yu, Y. Lou, C. Li, Y. Han, Z. Shi, S. Feng, 3D hierarchical ZnIn<sub>2</sub>S<sub>4</sub> nanosheets with Rich Zn vacancies boosting photocatalytic CO<sub>2</sub> Reduction, *Adv. Funct. Mater.* 29 (2019), 1905153, <https://doi.org/10.1002/adfm.201905153>.

[43] L. Wang, H. Tan, L. Zhang, B. Cheng, J. Yu, In-situ growth of few-layer graphene on ZnO with intimate interfacial contact for enhanced photocatalytic CO<sub>2</sub> reduction activity, *Chem. Eng. J.* 411 (2021), 128501, <https://doi.org/10.1016/j.cej.2021.128501>.

[44] L. Liu, H. Zhao, J.M. Andino, Y. Li, Photocatalytic CO<sub>2</sub> reduction with H<sub>2</sub>O on TiO<sub>2</sub> nanocrystals: comparison of anatase, rutile, and brookite polymorphs and exploration of surface chemistry, *ACS Catal.* 2 (2012) 1817–1828, <https://doi.org/10.1021/cs300273q>.

[45] X. Li, W. He, C. Li, B. Song, S. Liu, Synergetic surface modulation of ZnO/Pt@ZIF-8 hybrid nanorods for enhanced photocatalytic CO<sub>2</sub> valorization, *Appl. Catal. B: Environ.* 287 (2021), 119934, <https://doi.org/10.1016/j.apcatb.2021.119934>.

[46] J.D. Yi, R. Xie, Z.L. Xie, G.L. Chai, T.F. Liu, R.P. Chen, Y.B. Huang, R. Cao, Highly selective CO<sub>2</sub> electroreduction to CH<sub>4</sub> by in situ generated Cu<sub>2</sub>O single-type sites on a conductive MOF: stabilizing key intermediates with hydrogen bonding, *Angew. Chem. Int. Ed. Engl.* 59 (2020) 23641–23648, <https://doi.org/10.1002/anie.202010601>.

[47] H. Li, Y. Gao, Z. Xiong, C. Liao, K. Shih, Enhanced selective photocatalytic reduction of CO<sub>2</sub> to CH<sub>4</sub> over plasmonic Au modified g-C<sub>3</sub>N<sub>4</sub> photocatalyst under UV-vis light irradiation, *Appl. Surf. Sci.* 439 (2018) 552–559, <https://doi.org/10.1016/j.apsusc.2018.01.071>.

[48] H. Gao, P. Zhang, J. Zhao, Y. Zhang, J. Hu, G. Shao, Plasmon enhancement on photocatalytic hydrogen production over the Z-scheme photosynthetic heterojunction system, *Appl. Catal. B Environ.* 210 (2017) 297–305, <https://doi.org/10.1016/j.apcatb.2017.03.050>.

[49] H. Liu, G. Zhao, X. Meng, J. Ye, Doping Ba into strontium titanate for enhanced photocatalytic oxygen evolution over its supported Au-based catalysts, *Catal. Commun.* 99 (2017) 127–130, <https://doi.org/10.1016/j.catcom.2017.06.010>.

[50] O. Elbanna, S. Kim, M. Fujitsuka, T. Majima, TiO<sub>2</sub> mesocrystals composites with gold nanorods for highly efficient visible-NIR-photocatalytic hydrogen production, *Nano Energy* 35 (2017) 1–8, <https://doi.org/10.1016/j.nanoen.2017.03.014>.

[51] H.X. Han, C. Shi, N. Zhang, L. Yuan, G.P. Sheng, Visible-light-enhanced Cr(VI) reduction at Pd-decorated silicon nanowire photocathode in photoelectrocatalytic microbial fuel cell, *Sci. Total Environ.* 639 (2018) 1512–1519, <https://doi.org/10.1016/j.scitotenv.2018.05.271>.